Available online at www.sciencedirect.com

ScienceDirect

journal homepage: www.elsevier.com/locate/AJPS

Original Research Paper

Polydopamine-coated i-motif DNA/Gold nanoplatforms for synergistic photothermal-chemotherapy

Bo Chen [a,1], Lan Mei [a,1], Rangrang Fan [b], Di Chuan [a], Yangmei Ren [a], Min Mu [a], Haifeng Chen [b], Bingwen Zou [c], Gang Guo [a,*]

[a] State Key Laboratory of Biotherapy and Cancer Center, West China Hospital, Sichuan University, Chengdu 610041, China
[b] Department of Neurosurgery, West China Hospital, Sichuan University, Chengdu 610041, China
[c] Department of Thoracic Oncology and Department of Radiation Oncology, Cancer Center, West China Hospital, Sichuan University, Chengdu 610041, China

ARTICLE INFO

ABSTRACT

The combination of photothermal therapy with chemotherapy has gradually developed into promising cancer therapy. Here, a synergistic photothermal-chemotherapy nanoplatform based on polydopamine (PDA)-coated gold nanoparticles (AuNPs) were facilely achieved via the in situ polymerization of dopamine (DA) on the surface of AuNPs. This nanoplatform exhibited augmented photothermal conversion efficiency and enhanced colloidal stability in comparison with uncoated PDA shell AuNPs. The i-motif DNA nanostructure was assembled on PDA-coated AuNPs, which could be transformed into a C-quadruplex structure under an acidic environment, showing a characteristic pH response. The PDA shell served as a linker between the AuNPs and the i-motif DNA nanostructure. To enhance the specific cellular uptake, the AS1411 aptamer was introduced to the DNA nanostructure employed as a targeting ligand. In addition, Dox-loaded NPs (DAu@PDA-AS141) showed the pH/photothermal-responsive release of Dox. The photothermal effect of DAu@PDA-AS141 elicited excellent photothermal performance and efficient cancer cell inhibition under 808 nm near-infrared (NIR) irradiation. Overall, these results demonstrate that the DAu@PDA-AS141 nanoplatform shows great potential in synergistic photothermal-chemotherapy.

* Corresponding author.
  E-mail address: guogang@scu.edu.cn (G. Guo).
[1] These authors contributed equally to this work.
  Peer review under responsibility of Shenyang Pharmaceutical University.

1. Introduction

Cancer is still one of the most difficult diseases to treat, seriously endangering human health; therefore, finding an effective treatment method is of paramount importance. As one of the main methods of tumor treatment, traditional chemotherapy has disadvantages, such as poor targeting, strong side effects, and low availability, resulting in limited tumor treatment effects [1,2]. In recent years, photothermal therapy (PTT) has gradually become a new method of tumor treatment, in which nanomaterials convert the absorbed light into heat to ablate tumor cells [3–7]. Compared with traditional chemotherapy, PTT has the advantages of being minimally invasive, reducing patient pain, and shortening the treatment time. It is urgent to find a way to eliminate the harm of PTT to normal tissues [8,9]. At present, two methods have been proposed to reduce the damage to normal tissues caused by PTT, which not only provide a high anticancer effect but also guarantee the safety of nanoplatforms, including (1) improving the targeting ability of photosensitizers so that nanoparticles can be highly accumulated on tumor sites; (2) enhancing the photothermal conversion efficiency of nanoparticles, thereby reducing the laser power of near-infrared (NIR); and (3) applying low-temperature PTT to reduce heat resistance by inhibiting the synthesis of heat shock proteins to suppress cancer cells, reducing the temperature required for treatment [10–12].

Gold nanoparticles (AuNPs), with especially localized surface plasmon resonance (LSPR) and surface-enhanced Raman scattering (SERS), are widely used in tumor diagnosis and therapy [13–19]. In addition, the low toxicity, easy modification, and high photothermal conversion efficiency recommend AuNPs as excellent photosensitizers in PTT [20]. Bare AuNPs have poor colloidal stability and are prone to self-aggregation, limiting their biomedical application [21–25]. Therefore, great efforts have been made to improve the stability of AuNPs, such as the modification of DNA strands, polyethylene glycol (PEG), and polydopamine (PDA) [26–30].

Dopamine (DA) is a catecholamine neurotransmitter abundant in the brain that self-polymerizes to PDA under alkaline conditions [31]. The structure of PDA is similar to the nature of melanin, which is widely distributed in almost all organisms and contains abundant π electron clouds that can interact with other molecules containing π electron clouds [32]. At the same time, the structure of PDA contains active double bonds that can react with some groups (such as amino and sulfhydryl groups). Doxorubicin (Dox), an aromatic ring drug, can be loaded on the PDA shell *via* π-π stacking, electrostatic attraction, and hydrophobic interactions, suggesting the high drug-loading capacity of PDA-coated AuNPs. Owing to its excellent biocompatibility and high photothermal conversion efficiency, PDA has been explored for PTT. Taking advantage of spontaneous deposition on the substrate surface, PDA can readily adhere to the surface of AuNPs by covalent linkages or electrostatic interactions [33–35]. PDA-coated AuNPs not only enhance the photothermal effect of NPs and the stability of colloidal particles but also improve the drug-loading capacity of Dox.

In recent years, DNA nanotechnology has demonstrated great potential in biomedical areas, with applications ranging from drug delivery to biosensing and live imaging [36–41]. As an emerging field, DNA nanotechnology enables oligonucleotides to be well-defined shape nanostructures [42–44]. Moreover, functional DNA strands can be conjugated to other structures, such as inorganic nanoparticles and biopolymers. The differences in pH between intracellular and extracellular cancer cell environments are one of the key pathophysiological characteristics that provide the basis for the construction of pH-responsive nanocarriers [45]. The i-motif structure consisting of a cytosine-rich single-stranded DNA sequence can be folded into a C-quadruplex under acidic conditions [46]. Therefore, the pH-responsive i-motif structure has been applied to the fabrication of DNA-assisted nanocarriers [47].

In our previous study, pH-responsive DNA/AuNP nanocarriers were constructed for cancer therapy and exhibited good anticancer effects. However, there are some deficiencies that need to be solved, including the following: (1) the colloidal stability of DNA/AuNPs is easily affected by the ions in the solution; (2) the photothermal conversion efficiency of DNA/AuNPs needs to be enhanced, and the NIR laser power may cause damage to normal tissues. Thus, we designed PDA (shell)-coated AuNP (core) nanocarriers that could achieve good stability and excellent photothermal conversion efficiency.

In this study, we have developed a facile and versatile method to fabricate nanocarriers with excellent photothermal conversion, as well as high drug-loading capacity and long-term size stability. The inner AuNPs can serve as not only ideal photothermal agents but also as a framework for the polymerization of DA. PDA-coated AuNPs (DAu@PDA-AS141) with a uniform core-shell nanostructure were synthesized for synergistic photothermal-chemotherapy. As shown in Scheme 1, the hydrophilic polymer (SH-PEG$_{5000}$) was modified on the surface of AuNPs to enhance the size stability. Additionally, PDA-coated AuNPs (Au@PDA) with a thickness-tunable PDA shell were fabricated by the self-polymerization of DA on Au-PEG under alkaline conditions. Importantly, the numerous active double bonds of the PDA shell ensured modification with thiolated molecules. Then, thiolated i-motif DNA nanostructures were assembled on Au@PDA to obtain Au@PDA-AS141. Finally, Dox could be loaded on the GC base pairs of the DNA structure and PDA shell. This nanoplatform exhibited robust size stability and high photothermal conversion efficiency and achieved efficient cellular uptake as well as cancer inhibition. Taken together, this smart nanocarrier has shown the potential for synergistic photothermal-chemotherapy.

2. Materials and methods

2.1. *Materials*

Gold nanoparticles were purchased from XFNANO company (Nanjing, China). DNA oligonucleotides in this study were provided by Tsingke Bio. Tech. (Shanghai, China). Doxorubicin (Dox) and 3-[4,5 dimethylthiazol-2yl]-2,5-diphenyltetrazolium
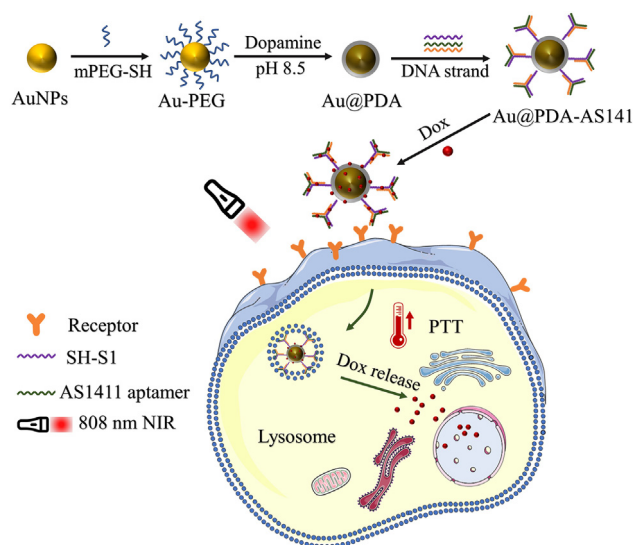
Scheme 1 – Schematic diagram of the synthesis of DAu@PDA-AS141 nanocarriers with enhanced photothermal conversion for synergistic photothermal-chemotherapy.

bromide (MTT) were purchased from Dalian Meilun Biotech Co., Ltd. (China). Tris(2-carboxyethyl)phosphine (TCEP) was purchased from Sigma–Aldrich (USA). SH-PEG$_{5000}$ was purchased from Ruixi Biological Technology (Xi'an, China). Phalloidin−fluorescein isothiocyanate (FITC) and 4,6-diamidino-2-phenylindole (DAPI) were purchased from Beyotime Biotechnology (Shanghai). Apoptosis assay kits and cell cycle kits were purchased from Becton Dickinson (USA).

2.2. Synthesis of DAu@PDA-AS141

SH-PEG$_{5000}$ was activated by adding TCEP to reduce the disulfide bond. Next, the activated SH-PEG$_{5000}$ (5 mg/ml) was mixed with 20-nm gold nanoparticles at the colling rate (37 °C to -10 °C, 1 °C/min). Then, Au-PEG was obtained after thawing and resuspended in Tris-HCl buffer (10 mM, pH 8.5). The PDA-coated gold nanoparticles were synthesized by mixing dopamine (1 mg/ml) and Au-PEG solution. The mixed solution was stirred at room temperature for 2 h, and the Au@PDA products were collected and washed three times with Milli-Q water by centrifugation (12,000 rpm, 20 min). The concentration of gold nanoparticles (DAu@PDA-AS141) was calculated by Lambert-Beer law: A=εbc (ε=2.4 × 10^8 l/mol/cm; b=1.0 cm), and the absorbance value (A) was measured at 520 nm by UV-vis.

To prepare Au@PDA-S1, the thiolated DNA strands (S1) were mixed with Au@PDA. After stirring at room temperature for 4 h, the Au@PDA-S1 NPs were washed three times and dispersed in PBS. Next, the Au@PDA-S1 NPs were mixed with complementary DNA strands (S2 and S3, sequences are listed in Table 1) and then annealed from 95 °C (5 min) to room temperature over 4 h. The Au@PDA-AS141 NPs were obtained after washing three times with Milli-Q water. To obtain DAu@PDA-AS141 NPs, 200 µl Dox (100 µM) solution was added to Au@PDA-AS141, followed by incubation for 2 h at 37 °C.

As a negative control, DAu@PDA-NEG NPs were synthesized as described above. The nontargeted DNA strands (S4 and S5) were mixed with Au@PDA-S1 and then annealed from 95 °C (5 min) to room temperature over 4 h to obtain Au@PDA-NEG. Then, 200 µl Dox (100 µM) solution was added to Au@PDA-NEG, followed by incubation for 2 h at 37 °C. Finally, DAu@PDA-NEG NPs were collected by centrifugation at 12,000 rpm for 20 min.

2.3. Characterization of nanoparticles

The hydrodynamic size, Zeta potential, and morphology were determined by dynamic light scattering (DLS, Malvern UK) and transmission electron microscopy (TEM, Hitachi H-600, Japan). The absorbance of different nanoparticles was determined using a UV–vis spectrophotometer (Shimadzu UV-2500). The fluorescence intensity of the nanoparticles was confirmed by a fluorescence spectrophotometer (Biotek Cytation 3, USA).

Agarose gel electrophoresis was used to verify that the DNA strands were successfully modified on the surfaces of the nanoparticles. The samples were separated by electrophoresis on a 1.0% agarose gel (1.0% agarose powder, TBE buffer containing 12.5 mM MgAc$_2$) at 100 V for 60 min. Then, the photos of agarose gels were obtained under a light-transmitting whiteboard.

2.4. Stability of nanoparticles

DAu@PDA-AS141 nanoparticles were stored at 4 °C at different times. At different time points, the size distribution of the NPs was determined by DLS to test the size stability.

2.5. The drug loading (DL) and encapsulation efficiency (EE) of nanoparticles

The supernatant of DAu@PDA-AS141 solution was collected by centrifuging at 15,000 rpm for 60 min, and the concentration of free Dox was monitored by absorption measurement at 480 nm by UV-vis.The calculation equation of drug loading efficiency (LE) and encapsulation efficiency (EE) were as follows:

$$DL (\%) = (\text{weight of Dox in the nanoparticles}/ \\ \text{total weight of nanoparticles}) \times 100\%$$

$$EE (\%) = (\text{weight of Dox in the nanoparticles}/ \\ \text{total weight of Dox in feed}) \times 100\%$$

2.6. In vitro drug release

DAu@PDA-AS141 NPs (2.0 ml) were placed in centrifuge tubes with different pH values (pH 5.5 and 7.4) in a 37°C water bath. For the PTT group, the samples were irradiated by 808 nm NIR (1.5 W/cm^2, 5 min) at specific time intervals. Then, the supernatant was collected by centrifugation (4°C, 12,000 rpm), and the concentration of released Dox was detected by UV–vis spectroscopy.

Table 1
DNA sequences referenced in this article.

Name	Sequence
S1	5'SH(CH2)$_6$TTTTTTTTTTCCCAACCCCACCACCCTACCCC
S2	TTGGTGGTGGTGGTTGTGGTGGTGGTGGTTTCGACTAAGCGAGTGGGGTTGGG
S3	TTGGTGGTGGTGGTTGTGGTGGTGGTGGTTTGGGGTAGGGTGTGGCTTAGTCG
S4	AATAATAATAATTATAATAATAATAATATTTCGACTAAGCGAGTGGGGTTGGG
S5	AATAATAATAATTATAATAATAATAATATTTGGGGTAGGGTGTGGCTTAGTCG
Cy5-S2	5'Cy5-TTGGTGGTGGTGGTTGTGGTGGTGGTGGTTTCGACTAAGCGAGT GGGGTTGGG
Cy5-S3	5'Cy5-TTGGTGGTGGTGGTTGTGGTGGTGGTGGTTTGGGGTAGGGTGT GGCTTAGTCG

2.7. Photothermal properties analysis

Briefly, 1.0 ml DAu@PDA-AS141 NP solutions with different concentrations (0.5, 1.0, 2.0 and 4.0 nM) were irradiated by 808 nm NIR (1.5 W/cm^2, 5 min), and the temperature was monitored. Additionally, the photothermal conversion performance of DAu@PDA-AS141 NPs under different NIR powers was investigated following the procedure mentioned above.

2.8. Cell culture

The mouse breast cancer cell line 4T1 was purchased from the American Type Culture Collection. The 4T1 cells were cultured in RPMI-1640 medium supplemented with 10% FBS (fetal bovine serum) and 1% penicillin–streptomycin solution at 37 °C with 5% CO$_2$.

2.9. In vitro wound healing assay

A wound healing assay was performed to assess the ability of nanocarriers to inhibit the migration of cancer cells. The 4T1 cancer cells were seeded in 12-well plates at a concentration of 1×10^5 cells per well and incubated overnight. Then, a sterile pipette was used to scratch the cell monolayer, and floating cells were removed by washing three times with PBS. Fresh medium samples containing free Dox, Dox@AuNP-AS141, and DAu@PDA-AS141 were added to the wells and incubated for 24 h. Microscopy was performed to obtain images of the wells.

2.10. Cellular uptake assays

4T1 cells were seeded in 12-well plates at a density of 2×10^5 cells/well for 24 h. Next, the cells were treated with DAu@PDA-AS141 for 1.0, 2.0, and 4.0 h with equal concentrations of Dox. Then, the cells were washed with PBS three times and detected by flow cytometry (FCM). The cellular uptake of nanoparticles was also evaluated by confocal laser scanning microscopy (CLSM), and 4T1 cells were cultured in 24-well plates with a preloaded glass slide at a concentration of 1×10^5 cells per well. Then, the cells were treated with DAu@PDA-NEG and DAu@PDA-AS141 for 1.0, 2.0, and 4.0 h with equal concentrations of Dox. The cells were washed with PBS three times and fixed with 4% paraformaldehyde. DAPI and β-actin

were used to stain 4T1 cells, and the cell slides were viewed by CLSM.

2.11. Cell cytotoxicity analysis

An MTT assay was used to evaluate the cytotoxicity of nanoparticles against 4T1 cancer cells. In brief, 4T1 cells were seeded in 96-well plates at a density of 4×10^3 cells per well for 24 h. Then, free Dox, Dox@AuNP-AS141, and DAu@PDA-AS141 with or without 808 nm NIR laser irradiation (1.5 W/cm^2, 5 min) were added to plates and incubated for another 24 h. The culture medium was replaced by fresh MTT (20 μl, 5 mg/ml) and incubated for 4 h. The absorbance of each sample was measured at 570 nm using a multifunctional microplate reader. The combination index (CI) was applied to evaluate the synergistic interaction between PTT and chemotherapy. And the computational formula of CI: $\text{CI} = \left[\text{IC}_{50 \text{ (combined therapy)}}/\text{IC}_{50 \text{ (chemotherapy alone)}}\right] + \left[\text{IC}_{50 \text{ (combined therapy)}}/\text{IC}_{50 \text{ (PTT alone)}}\right]$.

4T1 cells were seeded in 12-well plates at a concentration of 2×10^5 cells/well and incubated for 24 h. The cells were washed twice with PBS and cultured with medium containing free Dox, Dox@AuNP-AS141, and DAu@PDA-AS141. For the PTT group, the cells were irradiated with NIR (1.5 W/cm^2) for 5 min. After 48 h of culture, the cells were digested and washed. Then, the samples were stained with Annexin V-FITC/7AAD reagents and analyzed by FCM.

2.12. Cell cycle assays

4T1 cells were cultured in 12-well plates at a concentration of 4×10^5 cells/well and then incubated with free Dox, Dox@AuNP-AS141, and DAu@PDA-AS141. After incubation for 48 h, the cells were collected and fixed with 75% EtOH at 4 °C overnight. The cells were stained with propidium iodide/RNase (PI/RNase, 100 μl/well) for 30 min. Then, the cell cycle was analyzed by FCM.

2.13. In vivo antitumor study

Once the tumor volume of 4T1 tumor-bearing mice reached 100 mm3, the mices were intravenously injected with PBS, free Dox, DAu@PDA-NEG or DAu@PDA-AS141 (with or without 808 nm laser irradiation: 1.5 W/cm^2, 5 min; Dox: 5 mg/Kg).
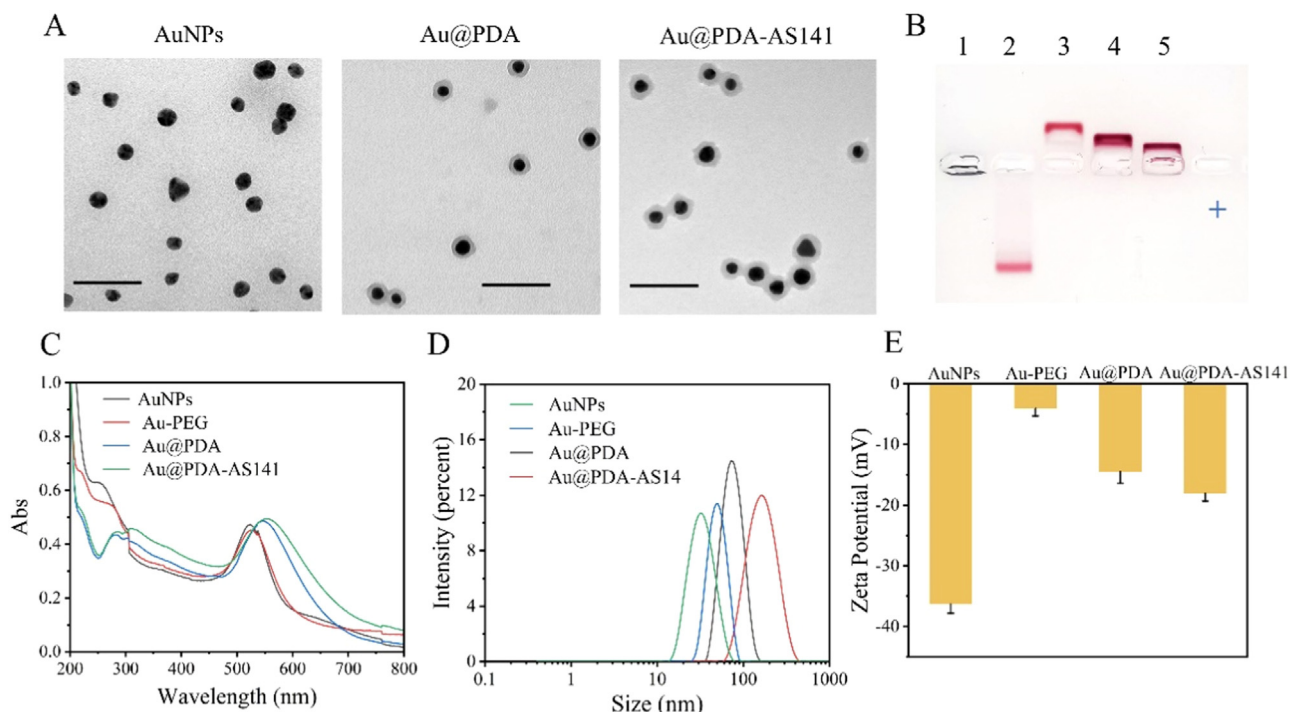
Fig. 1 – Morphology and structure of nanocarriers. (A) TEM images of different nanoparticles. The scale bar is 100 nm. (B) Agarose gel electrophoresis analysis of nanocarriers, Line 1: AuNPs; Line 2; AuNP-DNA; Line 3: Au-PEG; Line 4: Au@PDA-S1; Line 5: Au@PDA-AS141. (C) UV–vis absorption, (D) DLS characterization and (E) Zeta potential of nanocarriers.

The tumors were collected and stained with hematoxylin and eosin staining (H&E) and Ki67.

2.14. Statistical analysis

The experiments in this article were performed in triplicate, and the results are presented as the mean $\pm$ SD (standard deviation). Differences with $*P < 0.05$ were deemed significant.

3. Results and discussion

3.1. Size, Zeta potential, and morphology of nanoparticles

First, the morphology and structure of the NPs were determined by TEM. The uniform core-shell structure was formed by the spontaneous polymerization of DA on AuNPs, and the thickness of the PDA layer was approximately 10 nm, indicating the successful synthesis of Au@PDA. As shown in TEM images (Fig. 1A), the Au@PDA NPs had good dispersity and uniform average size. In addition, the thickness of the PDA shell could be tuned by the DA concentration, whereas an excess PDA layer could cause the aggregation of nanoparticles (Figs. S1 and S2). The size and surface charge of the nanoparticles were characterized by DLS. The size (28.1 $\pm$ 2.8 nm) and Zeta potential (-36.3 $\pm$ 1.5 mV) of citrate-capped AuNPs were consistent with a previous study (Fig. 1D and 1E). The average sizes of the nanoparticles increased to 94.3 $\pm$ 1.7 nm, 147 $\pm$ 2.6 nm, and 180 $\pm$ 2.6 nm, respectively. The attachment of PEG strands on AuNPs led to an increase

in the Zeta potential from -36.3 mV to -4.1 mV owing to charge screening. Furthermore, after the modification of the hydroxyl group on the AuNPs, lower Zeta potentials were observed for Au@PDA (-14.5 $\pm$ 1.9 mV) and Au@PDA-AS141 (-18.1 $\pm$ 1.3 mV) than for Au-PEG (-4.1 $\pm$ 1.2 mV). These results validated the successful synthesis of PDA-coated AuNPs and the functionalization of DNA nanostructures for further therapeutic applications.

3.2. UV–vis and agarose gel electrophoresis analysis

The LSPR peak of Au@PDA-AS141 was characterized by UV–vis absorption spectroscopy. As shown in Fig. 1C, the characteristic LSPR peaks of AuNPs, Au-PEG, Au@PDA, and Au@PDA-AS141 were located at 520 nm, 524 nm, 540 nm and 553 nm, respectively. The SH-PEG$_{5000}$ coating caused a slight redshift, while the PDA shell coating led to an obvious redshift, suggesting the successful assembly of Au@PDA. The obvious redshift of Au@PDA could be ascribed to the higher refractive index than that of water. Moreover, the increased absorbance at 258 nm was attributed to the characteristic peak of PDA. With the further assembly of the DNA nanostructure, the maximum absorbance of Au@PDA-AS141 increased to 553 nm.

In addition, agarose gel electrophoresis was used to demonstrate the successful assembly of PDA on AuNPs. The bare AuNPs easily aggregated at the origin point, and the color changed from red to black, showing poor dispersity (Fig. 1B). As the control, the DNA strand-modified AuNPs (AuNP-S1) exhibited good dispersity and migrated from the origin point. The negatively charged nanoparticles (AuNP-S1) migrated
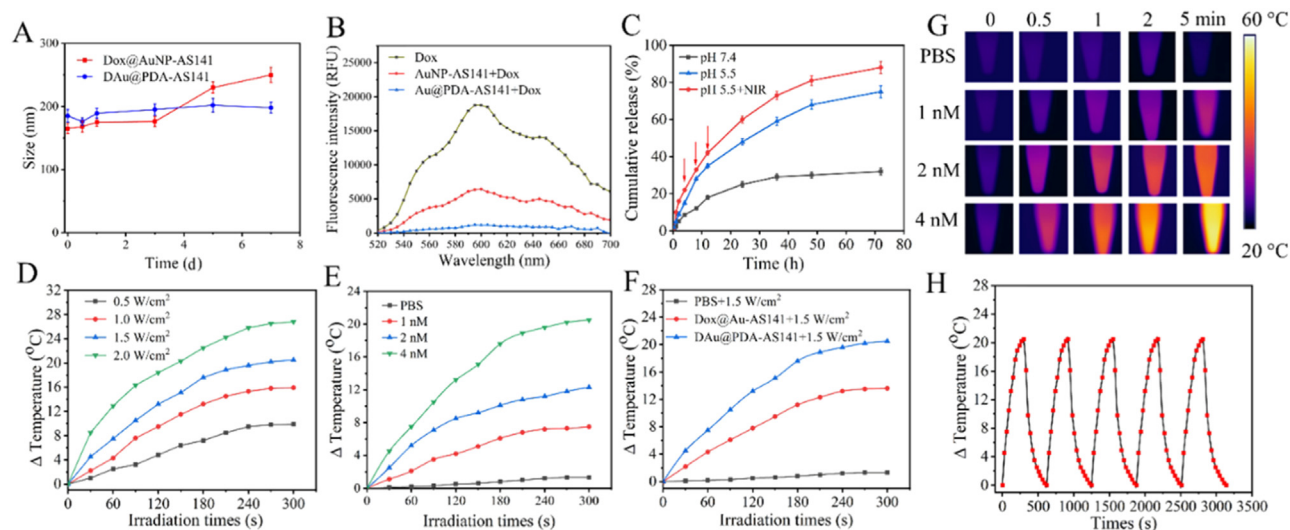
Fig. 2 – (A) Stability of nanoparticles. **(B)** Drug loading of Dox on AuNP-AS141 and Au@PDA-AS141. **(C)** Drug release of DAu@PDA-AS141 under different pH values and NIR irradiation, red arrows in the figure indicated a transient NIR irradiation (808 nm, 1.5 W/cm^2, 5 min).. Temperature elevation curves of DAu@PDA-AS141 under 808 nm NIR irradiation with different power densities**(D)** and different concentrations **(E)**. **(F)** Temperature elevation curves of DAu@PDA-AS141 and Dox@AuNP-AS141 under 808 nm NIR irradiation. **(G)** Thermal images and **(H)** photothermal stability of DAu@PDA-AS141 under 808 nm NIR irradiation.

from the negative electrode to the positive electrode. However, the Au-PEG NPs migrated from the positive electrode to the negative electrode though it was negatively charged, which was ascribed to the combined effects of coupling forces and hydrodynamic drag. The lower migration rates of Au@PDA and Au@PDA-AS141 than that of Au-PEG indicated that successful assembly of Au@PDA-AS141 was achieved.

3.3. Stability of nanoparticles

In the field of colloidal chemistry, the stability of colloidal AuNPs was maintained by charge repulsion between particles. Hence, the stability of AuNPs was easily affected by the salt ions in the solution, which could shield the electrostatic repulsion. The stability of AuNPs was improved after the modification of the DNA nanostructure because of the steric stabilization of polymers. However, the particle size of Dox@AuNP-AS141 after 3 proved that the particles aggregated irreversibly (Fig. 2A). In contrast, the stability of DAu@PDA-AS141 was significantly enhanced due to the stabilizing effect of the hydrophilic polymer (PEG) and PDA, and the size did not increase even after 7 days. DAu@PDA-AS141 remained stable in the solution and did not aggregate. In summary, the coating of PEG and PDA shells could effectively improve the stability of DAu@PDA-AS141.

3.4. Drug loading

Apart from enhancing the photothermal conversion of NPs, the PDA shell provided the sites for drug delivery. The Dox molecules could be loaded on the PDA shell by π-π stacking, and the successful loading of Dox was demonstrated by fluorescence spectroscopy. To prove that the PDA shell

could enhance the drug-loading capability of nanoparticles, AuNP-AS141 and Au@PDA-AS141 NPs were mixed with Dox solutions at the same concentration. As shown in Fig. 2B, the fluorescence intensity of Dox decreased sharply after the addition of AuNP-AS141, which was attributed to the fluorescence quenching induced by the interaction between Dox and GC base pairs. Moreover, the fluorescence intensity of Dox was further decreased after the addition of Au@PDA-AS141 and was lower than that of AuNP-AS141. Therefore, the coating of the PDA shell could improve the drug-loading capacity of NPs.

3.5. In vitro drug release profile of DAu@PDA-AS141

The Dox release profile of DAu@PDA-AS141 was related to the pH and NIR irradiation. The drug release profiles of DAu@PDA-AS141 were evaluated at different pH values with or without the NIR laser. A chemotherapy agent (Dox) was chosen as the model drug. As shown in Fig. 2C, after Dox was mixed with Au@PDA-AS141, the drug-loading capacity of DAu@PDA-AS141 was approximately 18% (w/w) and encapsulation efficiency (EE) was about 80%. Detailed drug release profiles revealed that approximately 71.2% of preloaded Dox could be released from DAu@PDA-AS141 in 72 h at pH 5.5, while only 30.1% of preloaded Dox could be released in 72 h at pH 7.4. The burst Dox release of DAu@PDA-AS141 under lower pH values could be ascribed to the pH-stimulated PDA and i-motif DNA structure. Note that the drug release of DAu@PDA-AS141 was increased to 88.3% in 72 h at pH 5.5 when exposed to NIR irradiation (1.5 W/cm^2, 5 min). The enhanced drug release could be attributed to the photothermal effect-induced temperature, which could promote the destruction of hydrogen bonds between DNA

double strands and weaken the interaction between Dox and PDA.

3.6. In vitro photothermal effects

The photothermal efficiencies of DAu@PDA-AS141 and Dox@AuNP-AS141 were investigated by real-time temperature changes under 808 nm NIR irradiation. As shown in Fig. 2D-2G, the photothermal performance of DAu@PDA-AS141 was dependent on concentration and laser power. The temperature change of the DAu@PDA-AS141 solution (2.0 nM) increased from 0 to 26.8 °C under 808 nm NIR irradiation (1.5 W/cm^2, 5 min). In contrast, the PBS group was used to demonstrate the safety of the NIR laser, and the temperature changes of the PBS group were maintained below 5°C under the same NIR laser power. Notably, DAu@PDA-AS141 showed a higher temperature than its control Dox@PDA-AS141, implying the enhanced photothermal conversion of DAu@PDA-AS141 (Fig. 2F). Moreover, the photothermal stability of DAu@PDA-AS141 was determined by five laser on/off cycles, and the highest temperature of Dau@PDA-AS141 did not show an obvious change (Fig. 2H).

3.7. Cellular uptake

To clarify the mechanism of cellular uptake, Dau@PDA-AS141 and Dau@PDA-NEG NPs were used for cellular uptake studies. The cellular uptake of NPs was the key step to achieving therapeutic application, which was confirmed by the FCM and CLSM results. The cellular uptake rates of free Dox and DAu@PDA-AS141 by 4T1 cancer cells were analyzed by FCM at different times. As observed in Fig. 3A, the cellular uptake rate of DAu@PDA-AS141 gradually increased when the incubation time increased from 1 h to 4 h, indicating the efficient internalization of nanoparticles. As shown in Fig. 3B, the red fluorescence of both DAu@PDA-AS141 and DAu@PDA-NEG displayed time-dependent behavior, and the red fluorescence of DAu@PDA-AS141 NPs was stronger than that of DAu@PDA-NEG NPs. Besides, the cellular uptake efficiency is effectively inhibited by chlorpromazine hydrochloride (CPZ), implying that clathrin-mediated endocytosis plays an important role in the internalization of DAu@PDA-AS141 (Fig. S4). Overall, the specific cellular uptake of DAu@PDA-AS141 was significantly augmented by modification with AS1411 aptamers.

4T1 cells were incubated with Au@PDA-AS141-Cy5 at an equivalent concentration to explore intracellular internalization and stained with Lyso-Tracker Green to study the colocalization of NPs and lysosomes. As shown in Fig. 3C and 3D, only a small portion of red fluorescence colocalized with green fluorescence at 1 h, indicating that few NPs were included in lysosomes. The red fluorescence of Au@PDA-AS141 mostly overlapped with the green fluorescence of lysosomes after incubation for 4 h. However, the overlapped yellow fluorescence (colocalization of red and green fluorescence) was drastically decreased after incubation for 6 h, which implied that Au@PDA-AS141 NPs escape the lysosomes and entered the cytoplasm. According to the colocalization analysis, the colocalization rates of Au@PDA-AS141 at different times were 0.16 (1 h), 0.30 (2 h),

0.71 (4 h), and 0.15 (6 h). Interestingly, the red fluorescence increased gradually with increasing time, suggesting that Au@PDA-AS141-Cy5 NPs were internalized by 4T1 cells via the receptor-mediated endocytic pathway. The amine group of the PDA shell can sequester protons and cause swelling and rupture of the lysosome. All these results verified that Au@PDA-AS141 NPs could escape from lysosomes and enter the cytoplasm.

3.8. Antimigration and cytotoxicity in vitro

Cancer cell migration is related to organ (e.g., liver and lung) metastasis. Herein, a wound healing assay was performed to assess cell migration. The migration distance was evaluated from the microscopy images. As shown in Fig. 4A and 4B, microscopy observations revealed that the artificial gap of the control group nearly disappeared after 24 h. 4T1 cells treated with free Dox showed a large migration distance (185 μm), while the DAu@PDA-AS141 group only migrated a short distance (80 μm). After NIR irradiation (1.5 W/cm^2, 5 min), the migration distance (56 μm) was lower than that of DAu@PDA-AS141 alone.

In addition, the viability of 4T1 cells treated with free Dox and DAu@PDA-AS141 with/without NIR irradiation was evaluated by MTT assays. As shown in Fig. 4C, DAu@PDA-AS141 exhibited significant concentration-dependent cytotoxicity, in which the cell viability was decreased to 20.7%. A more significant enhancement of cytotoxicity was observed under 808 nm NIR irradiation (the cell viability of DAu@PDA-AS141 with laser irradiation was further decreased to 14.5%). The IC$_{50}$ value of DAu@PDA-AS141 with laser irradiation was 3.06 μM and the CI value was calculated as 0.71, demonstrating the synergistic interaction between PTT and chemotherapy (Table S1). The normal cells (HUVECs) were used to verify the safety of the nanoplatform, and the Dox@PDA-AS141 and DAu@PDA-AS141 with or without laser irradiation did not show obvious toxicity (Fig. S6). These results indicated that chemotherapy combined with photothermal therapy could inhibit migration and enhance anticancer efficiency.

3.9. Cell apoptosis and cell cycle assays

The therapeutic efficiency of anticancer drugs depends on the ability to induce cell apoptosis, which is an orderly physiological process [48]. The anticancer mechanism of DAu@PDA-AS141 was quantified by a cell apoptosis assay. As shown in Fig. 5A and 5B, without NIR irradiation, the apoptosis percentages of 4T1 cells incubated with PBS, free Dox, DAu@PDA-NEG, and DAu@PDA-AS141 were 3.5% ± 0.6%, 32.13% ± 1.49%, 29.73% ± 2.31%, and 38.14% ± 2.15%, respectively. Compared with the nontargeted nanocarrier (DAu@PDA-NEG), the AS1411 aptamer-targeted nanocarrier (DAu@PDA-AS141) induced a higher rate of apoptosis. However, with NIR irradiation, the DAu@PDA-NEG and DAu@PDA-AS141 groups induced 41.01% ± 2.65% and 50.31% ± 1.87% apoptosis, respectively, revealing that the PDA shell coating enhanced the photothermal effect of the nanoparticles and that DAu@PDA-AS141 had the most efficient ability to induce apoptosis under NIR irradiation.
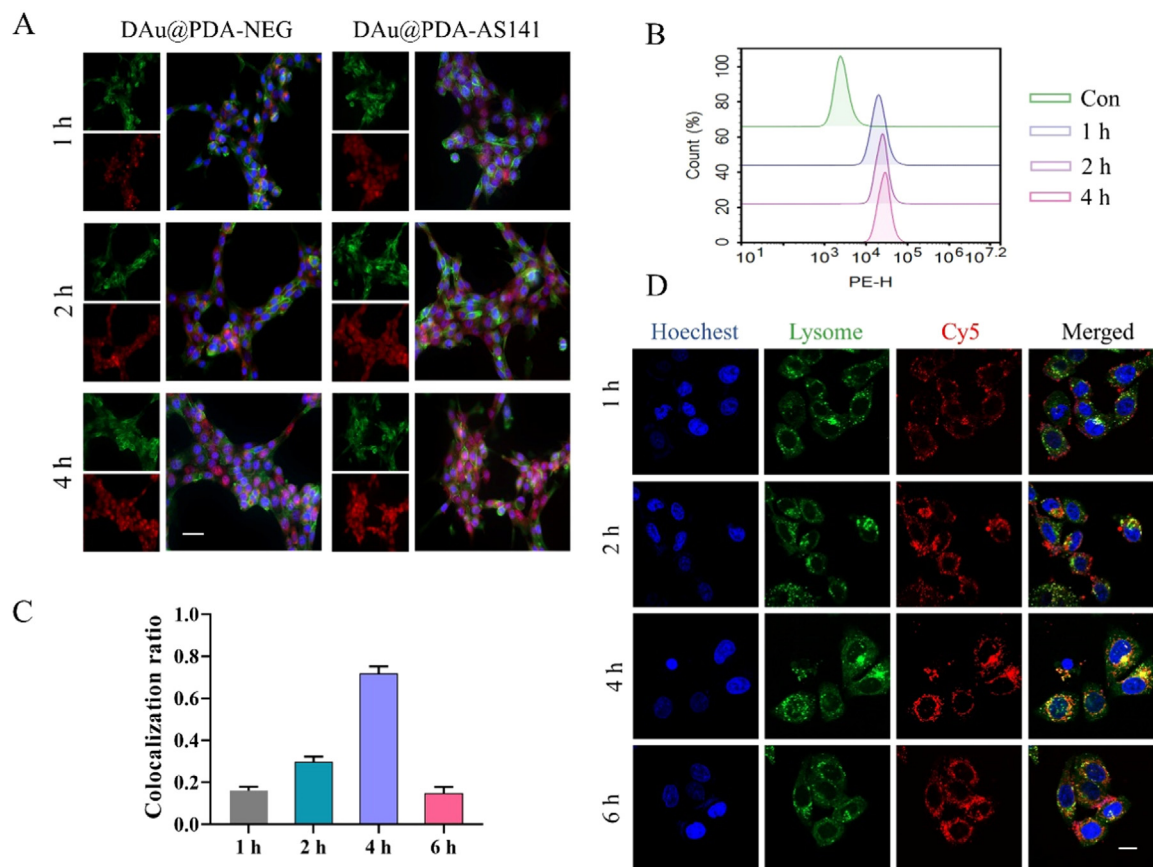
Fig. 3 – Cellular uptake of DAu@PDA-AS141 *in vitro*. (A) Flow cytometric assay of the cellular uptake of DAu@PDA-AS141 at different time points. (B) Confocal laser scanning microscopy images of DAu@PDA-AS141 and DAu@PDA-NEG. Blue: DAPI; Green: actin; Red: Dox. The scale bar is 20 μm. (C, D) Endolysosomal escape of Au@PDA-AS141-Cy5 at different time points. Blue: nuclei stained with Hoechst; Green: endolysosomes stained with LysoTracker Green; Red: red fluorescence of nanoparticles; Yellow: colocalization of Au@PDA-AS141 and endolysosomes. The scale bar is 10 μm.
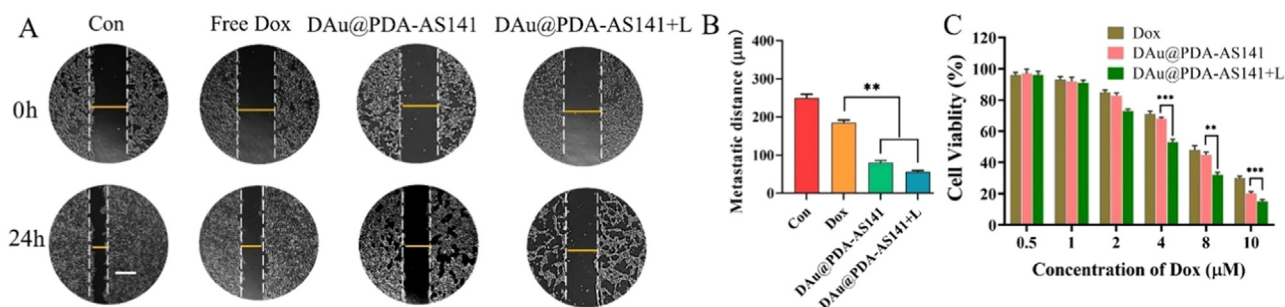
Fig. 4 – (A) Wound healing assay and (B) metastatic distance of 4T1 cells treated with Dox and DAu@PDA-AS141 with/without 808 nm NIR irradiation. The scale bar is 200 μm. (C) The viability of 4T1 cells treated with Dox and DAu@PDA-AS141 under 808 nm NIR irradiation. Error bars represent standard deviations, with n = 3 independent replicates: *$P < 0.05$, **$P < 0.01$, ***$P < 0.001$.

Taken together, synergistic photothermal-chemotherapy had a distinct advantage for 4T1 cancer cell killing.

Dox is a chemotherapeutic agent that shows an extremely wide anticancer spectrum by triggering cell cycle arrest [49]. The interactions among drugs, nanoparticles, and cancer cells were researched via cell cycle tests. As shown in Fig. 5C

and 5D, the proportions of cells in the G2/M phase after treatment with free Dox, DAu@PDA-NEG, and DAu@PDA-AS141 were 38.4%, 37.7% and 38.18%, respectively. In contrast, the nontargeted nanoparticles (DAu@PDA-NEG) only slightly increased the population of the G2/M phase, while the targeted nanoparticles (DAu@PDA-AS141) significantly
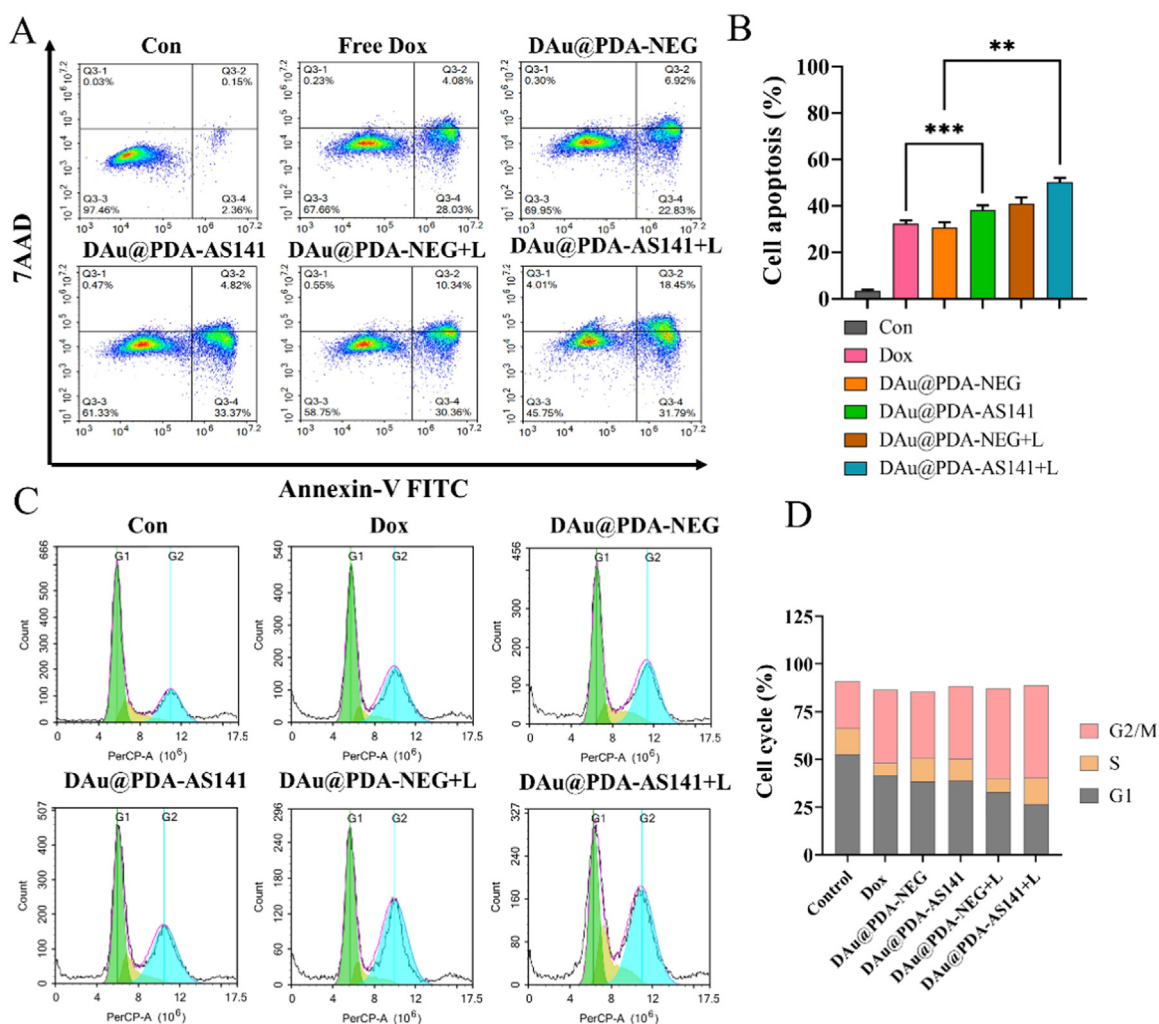
Fig. 5 – (A, B) Flow cytometry analysis of 4T1 cell apoptosis using Annexin V-FITC/7AAD assays. (C, D) Cell cycle test of 4T1 cells. Data are expressed as the mean ± SD. *$P < 0.05$, **$P < 0.01$, ***$P < 0.001$.

hindered the cell cycle in the G2/M phase. Similarly, with NIR irradiation, DAu@PDA-NEG (46.8%) and DAu@PDA-AS141 (48.9%) exhibited significant increases in the G2/M phase. Moreover, the induction of G2/M phase arrest was associated with programmed cell death.

3.10. In vivo anticancer effect

Tumor temperature was monitored by a thermal imager under 808 nm laser irradiation. As shown in Figs. 6A and S3, the tumor temperature of the DAu@PDA-AS141 group was approximately 52°C under NIR irradiation, indicating the strongest photothermal effect. In contrast, the PBS group had no photothermal effect. The synergistic therapeutic efficiency of DAu@PDA-AS141 was assessed by the detection of tumor volumes. The mice treated with Au@PDA-AS141 under laser irradiation showed successful elimination of tumors, which was ascribed to its excellent photothermal performance (Fig. 6B). The in vivo biodistribution showed that only a very weak signal was observed in mice treated with free Chlorin e6 (Ce6), whereas fluorescence increased gradually in the Cau@PDA-AS141 group (Fig. S5). As expected, the

tumor volume of DAu@PDA-AS141 in the NIR irradiation group was almost zero, which was even lower than the original volume (Fig. 6C). There was no apparent body weight decrease throughout the experimental period, implying that DAu@PDA-AS141 NPs exhibited good biocompatibility and no acute toxicity (Fig. 6D).

To further evaluate the anticancer effect of DAu@PDA-AS141, the tumor sections were stained with hematoxylin and eosin (H&E) and Ki67. The mice treated with DAu@PDA-AS141 NPs with NIR irradiation exhibited the most severe pathological damage in the tumor tissue. This histological examination was consistent with the in vitro results, which showed that the combined chemo-photothermal therapy induced a significant therapeutic effect (Fig. 6E). In addition, immunohistochemistry (IHC) staining was employed to estimate the effect of synergistic chemo-photothermal therapy. Tumor tissues were stained with a nuclear proliferation biomarker (Ki67) to assess tumor cell proliferation. The brown area in the DAu@PDA-AS141 with the NIR irradiation group was lower than that in the control group, indicating the remarkable inhibition of tumor development (Fig. 6F).
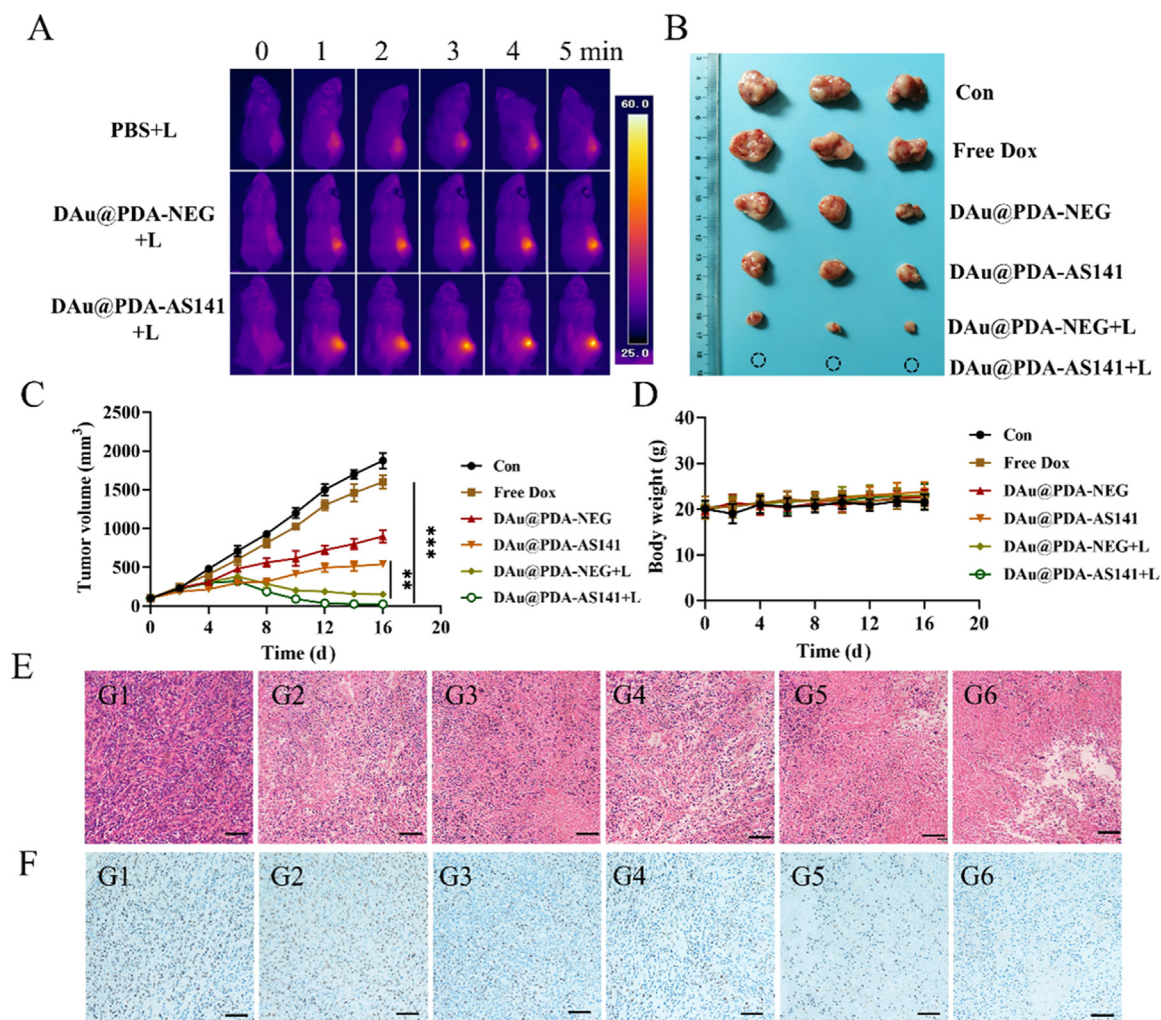
Fig. 6 – *In vivo* anticancer effect. (A) IR images of mice treated with different NPs with 808 nm laser irradiation (1.5 W/cm^2). (B) Images of tumors obtained from 4T1-bearing BALB/c mice after treatment. (C) Tumor volumes and (D) body weights of mice throughout the therapeutic process. (E) H&E and (F) Ki67 staining images of tumors after treatment. G1: PBS; G2: Free Dox; G3: DAu@PDA-NEG; G4: DAu@PDA-AS141; G5 DAu@PDA-NEG+L; G6: DAu@PDA-AS141+L; scale bar: 100 μm. Data are expressed as the mean ± SD. *P < 0.05, **P < 0.01, ***P < 0.001

H&E staining of major organs (heart, liver, spleen, lung, and kidney) was performed to estimate potential toxic effects (Fig. 7). Cardiotoxicity was observed in the free Dox group, which was consistent with previous reports. In addition, small liver metastasis nodules could be seen in the control and free Dox groups, and they could be significantly inhibited by DAu@PDA-AS141 with NIR irradiation, suggesting the suppression of metastasis. These results demonstrated that synergistic chemotherapy and photothermal therapy could enhance the anticancer effect in 4T1-bearing mice.

4. Conclusion

In conclusion, PDA-encased AuNPs for enhancing the photothermal conversion of nanocarriers were successfully developed for targeted photothermal chemotherapy. In addition, DAu@PDA-AS141 NPs with excellent photothermal effects and stability were synthesized by a facile and versatile method, which could be summarized as the self-polymerization of dopamine on the surface of AuNPs. After modification of the PEG and PDA shells, the obtained DAu@PDA-AS141 NPs exhibited a uniform core-shell nanostructure with good size distribution and long-term size stability. Compared with uncoated PDA NPs, the drug-loading capacity of PDA-coated NPs (DAu@PDA-AS141) was significantly improved due to the π-π stacking of PDA and Dox molecules. At the same time, Dox-loaded NPs (DAu@PDA-AS141) exhibited a characteristic pH-/photothermal-stimulated drug release. In the acidic environment, Au@PDA-AS141-Cy5 NPs were internalized by cancer cells via the receptor-mediated endocytic pathway and escaped from lysosomes and then entered the cytoplasm. After irradiation under 808 nm NIR, PDA-coated NPs (DAu@PDA-AS141) showed enhanced anticancer effects compared with single
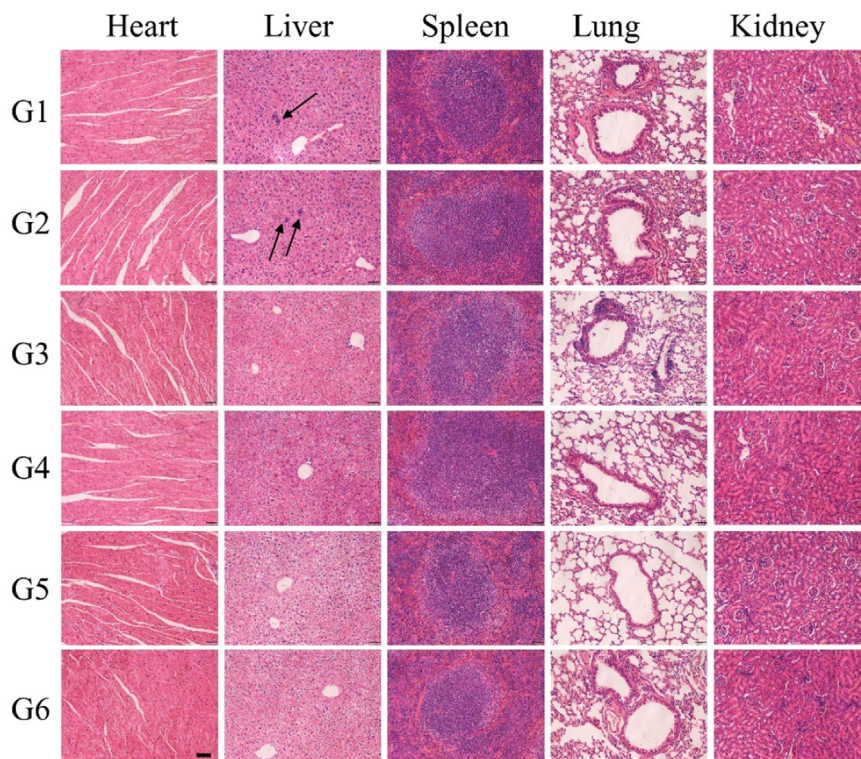
Fig. 7 – HE staining of the major organs (heart, liver, spleen, lung, and kidney). G1: PBS; G2: Free Dox; G3: DAu@PDA-NEG; G4: DAu@PDA-AS141; G5 DAu@PDA-NEG+L; G6: DAu@PDA-AS141+L; scale bar: 100 µm.

chemotherapy. The excellent photothermal conversion and high drug-loading capacity of the PDA-coated AuNPs indicated that they are strong candidates for synergistic photothermal-chemotherapy.

Conflicts of interest

The authors declare no competing interests.

Acknowledgments

Supplementary materials

Supplementary material associated with this article can be found, in the online version, at doi:10.1016/j.ajps.2023.100781.

References

[1] Jin Q, Zuo W, Lin Q, Wu T, Liu C, Liu N, et al. Zinc-doped Prussian blue nanoparticles for mutp53-carrying tumor ion interference and photothermal therapy. Asian J Pharm Sci 2022;17(5):767–77.

[2] Xu Q, Yang Y, Lu J, Lin Y, Feng S, Luo X, et al. Recent trends of mesoporous silica-based nanoplatforms for nanodynamic therapies. Coord Chem Rev 2022;469:214687.

[3] Fan X, Yue T, Liu A, Xie X, Fang W, Wei Y, et al. Lignin-assisted construction of sub-10 nm supramolecular self-assembly for photothermal immunotherapy and potentiating anti-PD-1 therapy against primary and distant breast tumors. Asian J Pharm Sci 2022;17(5):713–27.

[4] Shao J, Ruan C, Xie H, Li Z, Wang H, Chu PK, et al. Black-phosphorus-incorporated hydrogel as a sprayable and biodegradable photothermal platform for postsurgical treatment of cancer. Adv Sci 2018;5(5):1700848.

[5] Liang X, Mu M, Chen B, Chuan D, Zhao N, Fan R, et al. BSA-assisted synthesis of nanoreactors with dual pH and glutathione responses for ferroptosis and photodynamic synergistic therapy of colorectal cancer. Mater Today Adv 2022;16(3):100308.

[6] Zeng X, Luo M, Liu G, Wang X, Tao W, Lin Y, et al. Polydopamine-modified black phosphorous nanocapsule with enhanced stability and photothermal performance for tumor multimodal treatments. Adv Sci 2018;5(10): 1800510.

[7] Feng S, Lu J, Wang K, Di D, Shi Z, Zhao Q, et al. Advances in smart mesoporous carbon nanoplatforms for photothermal–enhanced synergistic cancer therapy. Chem Eng J 2022;435:134886.

[8] Li Z, Yang Y, Wei H, Shan X, Wang X, Ou M, et al. Charge-reversal biodegradable MSNs for tumor synergetic chemo/photothermal and visualized therapy. J Control Release 2021;338:719–30.

[9] Wang K, Lu J, Li J, Gao Y, Mao Y, Zhao Q, et al. Current trends in smart mesoporous silica-based nanovehicles for photoactivated cancer therapy. J Control Release 2021;339:445–72.

[10] Yang Y, Zhu WJ, Dong ZL, Chao Y, Xu L, Chen MW, et al. 1D Coordination polymer nanofibers for low-temperature photothermal therapy. Adv Mater 2017;29(40):12.

[11] Shu G, Shen L, Ding J, Yu J, Chen X, Guo X, et al. Fucoidan-based dual-targeting mesoporous polydopamine for enhanced MRI-guided chemo-photothermal therapy of HCC via P-selectin-mediated drug delivery. Asian J Pharm Sci 2022;17(6):908–23.

[12] Li Z, Yu Y, Zeng W, Ding F, Zhang D, Cheng W, et al. Mussel-inspired ligand clicking and ion coordination on 2D black phosphorus for cancer multimodal imaging and therapy. Small 2022;18(26):e2201803.

[13] Zhang Y, Mao X, Li F, Li M, Jing X, Ge Z, et al. Nanoparticle-assisted alignment of carbon nanotubes on DNA origami. Angew Chem Int Ed 2020;59(12):4892–6.

[14] Su J, Wang D, Norbel L, Shen J, Zhao Z, Dou Y, et al. Multicolor gold-silver nano-mushrooms as ready-to-use SERS probes for ultrasensitive and multiplex DNA/miRNA detection. Anal Chem 2017;89(4):2531–8.

[15] Yi Y, Kim HJ, Mi P, Zheng M, Takemoto H, Toh K, et al. Targeted systemic delivery of siRNA to cervical cancer model using cyclic RGD-installed unimer polyion complex-assembled gold nanoparticles. J Control Release 2016;244:247–56.

[16] Kapil N, Cardinale F, Weissenberger T, Trogadas P, Nijhuis TA, Nigra MM, et al. Gold nanoparticles with tailored size through ligand modification for catalytic applications. Chem Commun 2021;57(82):10775–8.

[17] Yang L, Kim TH, Cho HY, Luo J, Lee JM, Chueng SD, et al. Hybrid graphene-gold nanoparticle-based nucleic acid conjugates for cancer-specific multimodal imaging and combined therapeutics. Adv Funct Mater 2021;31(5):2006918.

[18] Zhu L, Lu Z, Zhang L, He N. Seedless synthesis of gold nanorods with tunable plasmonic peaks beyond 1300 nm. Chin Chem Lett 2022;33(5):2491–5.

[19] He P, Han W, Bi C, Song W, Niu S, Zhou H, et al. Many birds, one stone: a smart nanodevice for ratiometric dual-spectrum assay of intracellular microRNA and multimodal synergetic cancer therapy. ACS Nano 2021;15(4):6961–76.

[20] Wei Q, Arami H, Santos HA, Zhang H, Li Y, He J, et al. Intraoperative assessment and photothermal ablation of the tumor margins using gold nanoparticles. Adv Sci 2021;8(5):2002788 (Weinh).

[21] Wang G, Akiyama Y, Kanayama N, Takarada T, Maeda M. Directed assembly of gold nanorods by terminal-base pairing of surface-grafted DNA. Small 2017;13(44):1702137.

[22] Meng D, Ma W, Wu X, Xu C, Kuang H. DNA-driven two-layer core-satellite gold nanostructures for ultrasensitive microRNA detection in living cells. Small 2020;16(23):e2000003.

[23] Yamamoto S, Iwamaru Y, Shimizu Y, Ueda Y, Sato M, Yamaguchi K, et al. Epidermal growth factor-nanoparticle conjugates change the activity from anti-apoptotic to pro-apoptotic at membrane rafts. Acta Biomater 2019;88:383–91.

[24] Zhou H, Zhang J, Li B, Liu J, Xu JJ, Chen HY. Dual-Mode SERS and electrochemical detection of miRNA based on popcorn-like gold nanofilms and toehold-mediated strand displacement amplification reaction. Anal Chem 2021;93(15):6120–7.

[25] Huang P, Lian D, Ma H, Gao N, Zhao L, Luan P, et al. New advances in gated materials of mesoporous silica for drug controlled release. Chin Chem Lett 2021;32(12):3696–704.

[26] He MQ, Chen S, Meng J, Shi W, Wang K, Yu YL, et al. Capping ligand size-dependent LSPR property based on DNA nanostructure-mediated morphological evolution of gold nanorods for ultrasensitive visualization of target DNA. Anal Chem 2020;92(10):7054–61.

[27] Yin B, Ho LWC, Liu S, Hong H, Tian XY, Li H, et al. Sub-10 nm Substrate roughness promotes the cellular uptake of nanoparticles by upregulating endocytosis-related genes. Nano Lett 2021;21(4):1839–47.

[28] Huo SD, Gong NQ, Jiang Y, Chen F, Guo HB, Gan YL, et al. Gold-DNA nanosunflowers for efficient gene silencing with controllable transformation. Sci Adv 2019;5(10):eaaw6264.

[29] Petrushev B, Boca S, Simon T, Berce C, Frinc I, Dima D, et al. Gold nanoparticles enhance the effect of tyrosine kinase inhibitors in acute myeloid leukemia therapy. Int J Nanomedicine 2016;11:641–60.

[30] Chen B, Mei L, Fan R, Wang Y, Nie C, Tong A, et al. Facile construction of targeted pH-responsive DNA-conjugated gold nanoparticles for synergistic photothermal-chemotherapy. Chin Chem Lett 2021;32(5):1775–9.

[31] Wu B, Sun Z, Wu J, Ruan J, Zhao P, Liu K, et al. Nanoparticle-stabilized oxygen microcapsules prepared by interfacial polymerization for enhanced oxygen delivery. Angew Chem Int Ed 2021;60(17):9284–9.

[32] Fan R, Chen C, Hou H, Chuan D, Mu M, Liu Z, et al. Tumor acidity and near-infrared light responsive dual drug delivery polydopamine-based nanoparticles for chemo-photothermal therapy. Adv Funct Mater 2021;31(18):200793.

[33] Liu Y, Li Z, Yin Z, Zhang H, Gao Y, Huo G, et al. Amplified photoacoustic signal and enhanced photothermal conversion of polydopamine-coated gold nanobipyramids for phototheranostics and synergistic chemotherapy. ACS Appl Mater Interfaces 2020;12(13):14866–75.

[34] Choi CKK, Chiu YTE, Zhuo X, Liu Y, Pak CY, Liu X, et al. Dopamine-mediated assembly of citrate-capped plasmonic nanoparticles into stable core-shell nanoworms for intracellular applications. ACS Nano 2019;13(5):5864–84.

[35] Yamagishi K, Kirino I, Takahashi I, Amano H, Takeoka S, Morimoto Y, et al. Tissue-adhesive wirelessly powered optoelectronic device for metronomic photodynamic cancer therapy. Nat Biomed Eng 2019;3(1):27–36.

[36] Zhao J, Gao J, Xue W, Di Z, Xing H, Lu Y, et al. Upconversion luminescence-activated DNA nanodevice for ATP sensing in living cells. J Am Chem Soc 2018;140(2):578–81.

[37] Di Z, Zhao J, Chu H, Xue W, Zhao Y, Li L. An Acidic-microenvironment-driven DNA nanomachine enables specific ATP imaging in the extracellular milieu of tumor. Adv Mater 2019;31(33):e1901885.

[38] Woods D, Doty D, Myhrvold C, Hui J, Zhou F, Yin P, et al. Diverse and robust molecular algorithms using reprogrammable DNA self-assembly. Nature 2019;567(7748):366–72.

[39] Xiao M, Lai W, Wang F, Li L, Fan C, Pei H. Programming drug delivery kinetics for active burst release with DNA toehold switches. J Am Chem Soc 2019;141(51):20354–64.

[40] Cremers GAO, Rosier B, Ab M, Tito NB, van Duijnhoven SMJ, van Eenennaam H, et al. Determinants of ligand-functionalized DNA nanostructure-cell interactions. J Am Chem Soc 2021;143(27):10131–42.

[41] Mei L, Chen B, Fan R, Wu M, Weng C, Tong A, et al. Magic of architecting oligo-DNAs: 3D structure-dependent stability and programmable specificity to tumor cells. Adv Funct Mater 2022;32(18):2112544.

[42] Wei B, Dai M, Yin P. Complex shapes self-assembled from single-stranded DNA tiles. Nature 2012;485(7400):623–6.

[43] Yang J, Meng Z, Liu Q, Shimada Y, Olsthoorn RCL, Spaink HP, et al. Performing DNA nanotechnology operations on a zebrafish. Chem Sci 2018;9(36):7271–6.

[44] Chen B, Mei L, Wang Y, Guo G. Advances in intelligent DNA nanomachines for targeted cancer therapy. Drug Discov Today 2020;26(4):1018–29.

[45] Sun G, Du Y, Cui Y, Wang J, Li X, Tang A, et al. Terminal deoxynucleotidyl transferase-catalyzed preparation of pH-responsive DNA nanocarriers for tumor-targeted drug delivery and therapy. ACS Appl Mater Interfaces 2019;11(16):14684–92.

[46] Ma W, Chen B, Zou S, Jia R, Cheng H, Huang J, et al. I-motif-based *in situ* bipedal hybridization chain reaction for specific activatable imaging and enhanced delivery of antisense oligonucleotides. Anal Chem 2019;91(19):12538–45.

[47] Zhu JH, Kim Y, Lin HX, Wang SZ, Mirkin CA. pH-Responsive Nanoparticle Superlattices with Tunable DNA Bonds. J Am Chem Soc 2018;140(15):5061–4.

[48] Xue C, Hu S, Gao ZH, Wang L, Luo MX, Yu X, et al. Programmably tiling rigidified DNA brick on gold nanoparticle as multi-functional shell for cancer-targeted delivery of siRNAs. Nat Commun 2021;12(1):2928.

[49] Kregel S, Bagamasbad P, He S, LaPensee E, Raji Y, Brogley M, et al. Differential modulation of the androgen receptor for prostate cancer therapy depends on the DNA response element. Nucleic Acids Res 2020;48(9):4741–55.